

# Green Chemistry

Accepted Manuscript



This article can be cited before page numbers have been issued, to do this please use: S. Hernandez, C. Ottone, S. Proto, K. Tolod, M. Díaz de los Bernardos, A. Solé-Daura, J. J. Carbó, C. Godard, S. Castellón, N. Russo, G. Saracco and C. Claver, *Green Chem.*, 2017, DOI: 10.1039/C7GC00125H.



This is an Accepted Manuscript, which has been through the Royal Society of Chemistry peer review process and has been accepted for publication.

Accepted Manuscripts are published online shortly after acceptance, before technical editing, formatting and proof reading. Using this free service, authors can make their results available to the community, in citable form, before we publish the edited article. We will replace this Accepted Manuscript with the edited and formatted Advance Article as soon as it is available.

You can find more information about Accepted Manuscripts in the [author guidelines](#).

Please note that technical editing may introduce minor changes to the text and/or graphics, which may alter content. The journal's standard [Terms & Conditions](#) and the ethical guidelines, outlined in our [author and reviewer resource centre](#), still apply. In no event shall the Royal Society of Chemistry be held responsible for any errors or omissions in this Accepted Manuscript or any consequences arising from the use of any information it contains.

# New Core-Substituted Naphtalenediimides anchored on BiVO<sub>4</sub> for Visible Light-Driven Water Splitting

View Article Online  
DOI: 10.1039/C7GC00125H

Simelys Hernández,<sup>a,b,\*</sup> Carminna Ottone,<sup>c</sup> Stefano Proto,<sup>d</sup> Kristhine Tolod,<sup>a</sup>  
Miriam Díaz de los Bernardos,<sup>d</sup> Albert Solé-Daura,<sup>e</sup> Jorge J. Carbó,<sup>e</sup> Cyril  
Godard,<sup>e</sup> Sergio Castellón,<sup>f</sup> Nunzio Russo,<sup>a</sup> Guido Saracco,<sup>b</sup> Carmen Claver,<sup>d,e\*</sup>

<sup>a</sup> CREST group, Department of Applied Science and Technology (DISAT), Politecnico di Torino, Corso Duca degli Abruzzi 24, 10129 Turin, Italy.

<sup>b</sup> Center for Sustainable Future Technologies (CSFT@Polito), Italian Institute of Technology, Corso Trento 21, 10129, Turin, Italy.

<sup>c</sup> School of Biochemical Engineering, Pontificia Universidad Católica de Valparaíso. Av. Brasil 2085, Valparaíso, Chile.

<sup>d</sup> Centre Tecnològic de la Química a Catalunya (CTQC), CarrerMarcel·lí Domingo s/n, Edifici N5, 43007, Tarragona, Spain.

<sup>e</sup> Departament de Química Física i Inorgànica, Universitat Rovira i Virgili, CarrerMarcel·lí Domingo s/n, 43007, Tarragona, Spain.

<sup>f</sup> Department of Química Analítica i Química Orgànica, Universitat Rovira i Virgili, CarrerMarcel·lí Domingo s/n, 43007, Tarragona, Spain.

\*corresponding authors: E-mail: [simelys.hernandez@polito.it](mailto:simelys.hernandez@polito.it), [carmen.claver@ctqc.org](mailto:carmen.claver@ctqc.org)

## Abstract

In this work, a novel catalytic system for the sunlight-driven water splitting, which exploits the photocatalytic ability of BiVO<sub>4</sub> coupled to a new kind of noble-metal-free organic dye molecules, is proposed. Hence, mono- and di-substituted naphtalenediimides (NDIs), were designed to have different functional groups that provide to them both tunable optical properties and adjustable HOMO/LUMO levels, and were selectively prepared (starting from 1,4,5,8-naphthalenetetracarboxylic acid) achieving yields > 69 %. Smart anchoring groups (*i.e.* carboxylates or aromatic amines) were added to the dyes in order to allow them to covalently bond to acidic -OH groups present on the BiVO<sub>4</sub> surface. An easy and low-cost room temperature dip-coating technique was used to dye-sensitize both BiVO<sub>4</sub> powders and thin films. NMR, MS, FT-IR, TG, FESEM, XRD, XPS and optical analyses confirmed the successful organic synthetic routes and good dyes/BiVO<sub>4</sub> linkages. Photochemical and photoelectrochemical water oxidation reaction tests, together with DFT calculations, demonstrated that a proper alignment of the semiconductor/NDI-based dye energy levels is fundamental for enhancing the photocatalyst performance through a Z-scheme mechanism. The ability of the NDIs organic molecules to delocalize the electronic charges was also a key factor for minimizing recombination processes and achieving more than a ten-fold increase in the photocurrent density of a 6 cm<sup>2</sup> BiVO<sub>4</sub> photo-

electrode. The here reported results opens new perspectives for the utilization of this new series of core-substituted NDIs, which are able to improve photocatalysts activity for different sunlight-driven applications, e.g. waste water treatment and organic contaminants degradation, other than the production of solar fuels by water splitting mechanisms.

Keywords: Naphtalenediimides,  $\text{BiVO}_4$ , photocatalysis, water splitting, DFT, dye-sensitized semiconductor, EIS; Z-scheme.

## 1. Introduction

Light driven water-splitting into  $\text{H}_2$  and  $\text{O}_2$  is a topic of current interest,<sup>1-3</sup> and the development of a photocatalyst that can utilize the entire electromagnetic spectrum, in order to enhance the overall efficiency of the process, is nowadays a challenging problem.<sup>4</sup> In this context, bismuth vanadate ( $\text{BiVO}_4$ ) has recently gained increasing attention for its use as a photo-anode capable of promoting the oxidation of water to  $\text{O}_2$  in the half reaction of a complete PEC cell.<sup>5-8</sup>  $\text{BiVO}_4$  is one of the most promising photocatalyst for the oxygen evolution reaction (OER) because of its relatively low band gap of 2.4 eV<sup>9</sup> for the monoclinic phase, which enables a more efficient use of visible light, and due to the adequate position of the conduction and valence bands compared to the potential of water oxidation. Moreover,  $\text{BiVO}_4$  is nontoxic and is composed of relatively abundant elements. Regardless of the above quoted advantages provided by this inorganic semiconductor, bare  $\text{BiVO}_4$  powders and photo-anodes have usually proved relatively poor performances for photochemical and photoelectrochemical (PEC)  $\text{O}_2$  evolution due to slow  $\text{O}_2$  evolution kinetics, slow electron transport in the conduction band and, additionally, a significant electron-hole recombination at both bulk and surface.<sup>10</sup>

Several attempts have been performed in order to obtain optimum crystal structures and morphologies that are capable of enhancing the oxygen evolution activity of  $\text{BiVO}_4$ .<sup>11-15</sup> Morphology control (heterojunction, homojunction, nanocasting, etc.)<sup>16-18</sup> and doping techniques<sup>19-22</sup> have been investigated with the aim to enhance the  $\text{BiVO}_4$  photocatalytic efficiency by improving both surface area and electron/hole mobility, which are necessary to minimize recombination losses and facilitate the superficial charge transfer.

An alternative of this is the sensitization of the photocatalysts in order to use part of the solar spectrum that would not be exploited otherwise. In order to warrant a good electron/hole transfer between a sensitizer and the photocatalyst, the lowest unoccupied molecular orbital (LUMO) and the highest occupied molecular orbital (HOMO) of the dye must have higher energy than the conduction band (CB) and valence band (VB) of the semiconductor, respectively. Regarding the last approach, several configurations for noble-metal-containing dyes have been reported (e.g.

Ru, Rh- or Pd containing dyes).<sup>23, 24</sup> However, few metal-free dyes have been reported as efficient sensitizers for water splitting.<sup>25, 26</sup> Besides, surface functionalization could represent a more powerful and, at the same time, easily tunable approach able to improve the activity of BiVO<sub>4</sub>. Indeed, recent developments in this context deals with the use of functionalized carbon dots (CDs) for sensitizing semiconductor photo-electrodes.<sup>27, 28</sup> Recently, the photocatalytic enhancement of semiconductor based (*i.e.* TiO<sub>2</sub>) materials impregnated with a visible active polymer, *i.e.* polyaniline have also been reported.<sup>29</sup> Nevertheless, investigations concerning the use of organic visible-light active species to provide dye-sensitized systems have received less attention so far. Although Ru complex photosensitizers have shown very impressive conversion efficiency, their large-scale application is limited because of costs and environmental issues. In this context, metal-free organic dyes present many advantages, such as large molar extinction coefficient, control of absorption wavelength, facile design and synthesis, and lower cost that make them competitive with noble-metal-based complexes, in the near future.

In this work, we report our efforts toward the preparation of a novel catalytic system for light-driven OER, which combines the proven ability of the inorganic BiVO<sub>4</sub> in photochemical transformations with an organic visible-light active species, *i.e.* core substituted naphthalenediimides (NDIs). Four mono- and di-substituted NDIs were selectively prepared with 1,4,5,8-naphthalenetetracarboxylic acid as precursor. An appropriate control of the reaction conditions, including bromination, condensation and bromide substitution, were performed in order to obtain four metal-free dyes having different functional groups, which provide them tunable optical properties (for an efficient light-harvesting of all the solar spectra) and adjustable HOMO/LUMO levels. BiVO<sub>4</sub>, both powder and films, were impregnated with the dyes in order to investigate the effect of the dyes on the photocatalytic responses. BiVO<sub>4</sub> powder and photoanodes were prepared by previously optimized hydrothermal<sup>30</sup> and spin-coating<sup>6</sup> techniques, respectively. The photocatalytic activity of BiVO<sub>4</sub> impregnated with four different NDIs was proven by evaluating both their photocatalytic and photoelectrochemical behavior for the OER from water splitting under simulated sunlight irradiation. Their physico-chemical properties of all the prepared heterostructures were fully characterized, as well.

## 2. Experimental Section

### 2.1. Syntheses of core-substituted naphthalenediimides (NDIs)

#### 2.1.1. General.

Solvents and reagents were obtained from commercial sources (Sigma-Aldrich and Alfa-Aesar), unless otherwise stated, and were purified and dried according to standard procedures.<sup>31</sup> Air

sensitive reactions were carried out under argon in dry solvents and glassware. Flash column chromatography was carried out using a forced flow of the indicated solvent on Merck silica gel 60 (230–400 mesh). Reactions were monitored by TLC carried out on 0.25 mm E. Merck silica gel 60 F<sub>254</sub> glass or aluminum plates. Multinuclear NMR spectra were recorded on a Varian Mercury 400 MHz instrument. Chemical shift values for <sup>1</sup>H and <sup>13</sup>C were referred to internal SiMe<sub>4</sub> (0.0 ppm). Significant peaks are tabulated in the order: multiplicity (**s**, singlet; **d**, doublet; **t**, triplet; **q**, quartet; **m**, multiplet; **br s**, broad singlet), coupling constant(s) in Hertz (Hz) and number of protons. High resolution electrospray mass spectra (HR-ESI) were collected in positive mode on a MAT95XL from Thermo Finnigan. Matrix assisted laser desorption mass spectrometry analyses were performed on a BrukerBiflex III MALDI-TOF spectrometer using dithranol as matrix. The instrument was equipped with a nitrogen laser emitting at 337 nm, a 2 GHz sampling rate digitizer, a pulsed ion extraction source and a reflectron. Fourier transform infrared (FT-IR) spectra were recorded in pressed ATR mode on a Bruker Vector 22 spectrometer. TGA experiments were performed by using the furnace of a Mettler Toledo TGA/SDTA851 instrument. X-ray powder diffraction (XRD) spectra were recorded using a Siemens EM-10110BU D5000 diffractometer.

The synthetic strategy for the preparation of substituted-naphthalenediimides (**dyes 1 to 4**) is schematized in the Fig. 1 and explained in the following sections 2.1.2 to 2.1.7.

#### 2.1.2. *Dye 1: N,N'-dipyridyl 1,4,5,8-naphthalenetetracarboxylic acid dianhydride*

As shown in Fig. 1 (i), a mixture of 1,4,5,8-naphthalenetetracarboxylic acid dianhydride (0.8 g, 3 mmol) and 4-aminopyridine (0.56 g, 6 mmol) in anhydrous DMF (20 mL) was heated under reflux for 8 h. When the reaction mixture reached room temperature (r.t.), a crystalline solid precipitated out, which was collected by filtration. The crude product was purified by several recrystallization from DMF to obtain the pure compound named **dye 1** as pale yellow-orange needles (876 mg, 69% of yield).

#### 2.1.3. *2,6-Dibromo-1,4,5,8-naphthalenetetracarboxylic acid dianhydride (Br,Br-NDA)*

As shown in Fig. 1 (ii), a solution of dibromoisocyanuric acid (2.86 g, 10.0 mmol) in oleum (20 % SO<sub>3</sub>, 50 mL) was added at room temperature to a solution of naphthalene dianhydride (2.68 g, 10.0 mmol) in oleum (20 % SO<sub>3</sub>, 100 mL) over a period of 4 h. The resulting mixture was stirred at r.t. for 1 h, then cautiously poured onto crushed ice (500 g) to give a bright yellow precipitate. Water (1.5 L) was added, and the mixture was allowed to stand overnight at r.t. The yellow solid was collected on a Büchner funnel and dried at air providing the crude product, which was used for the next step without further purification. As it was not possible to purify at this stage, we assumed quantitative formation. Mp: >350 °C. Due to its extremely low solubility, no NMR spectrum could be obtained. It is worth to mention that batch-to-batch differences in the ratio of

mono-, di- and tetra-Br NDAs were noticed, which seemed to reflect the sensitivity of this reaction with respect to the concentration of the SO<sub>3</sub> in oleum.

*2.1.4. N,N'-Di-(2,6-diisopropylphenyl)-2,6-dibromonaphthalene-1,4,5,8-tetracarboxylic acid bisimide (Br,Br-NDI)*

As shown in Fig. 1 (iii), a mixture containing 2,6-Dibromonaphthalene-1,4,5,8-tetracarboxylic acid dianhydride (601.6 mg, 1.41 mmol) was suspended in acetic acid (30 mL) and heated at reflux for 30 min. Freshly distilled 2,6-Diisopropylaniline (1.6 mL, 8.47 mmol) was added dropwise and the mixture was kept at reflux at 120 °C for 30 min. The solution was poured into a mixture of crushed ice and distilled water and allowed to stand for 2 h at r.t. The red solid was collected on a Büchner funnel, dried at the 60 °C for 2 h and then purified on silica gel column chromatography(hexanes:Et<sub>2</sub>O98:2) to give the desired compound as a red-orange solid (205 mg, 20% yield).

*2.1.5. Dye 2: N,N'-Di-(2,6-diisopropylphenyl)-2-aminobenzoic acid-6-bromonaphthalene-1,4,5,8-tetracarboxylic acid bisimide (Br,N-NDI)*

For reaction (iv)(Fig. 1), in a 25 mL Schlenk-flask purged with Argon a mixture of *N,N'*-Di-(2,6-diisopropylphenyl)-2,6-dibromonaphthalene-1,4,5,8-tetracarboxylic acid bisimide (*Br,Br-NDI*) (71 mg, 0.095 mmol) and 4-aminobenzoic acid (131 mg, 0.956mmol) in 3 mL anhydrous DMF was stirred at 135 °C. The clear red solution turned deep violet after 2 h and was cooled to room temperature before quenching with aqueous saturated NaHCO<sub>3</sub>. The aqueous layer was extracted with DCM (3 x 100 mL) and the combined organic extracts were dried over MgSO<sub>4</sub>, filtered and concentrated under reduced pressure. The resulting waxy material was placed under high vacuum until DMF was completely removed and a violet-blue solid was obtained. Purification by column chromatography on silica gel (DCM:MeOH 9:1) provided **dye 2** as a violet solid (71 mg, 93 %).

*2.1.6. Dye 3: N,N'-Di-(2,6-diisopropylphenyl)-2-aminobenzoic acid-6-dimethylamine-naphthalene-1,4,5,8-tetracarboxylic acid bisimide (N,N-NDI)*

For reaction (v) (Fig. 1), in a 25 mL Schlenk-flask purged with Argon a mixture of *N,N'*-Di-(2,6-diisopropylphenyl)-2,6-dibromonaphthalene-1,4,5,8-tetracarboxylic acid bisimide (*Br,Br-NDI*) (40 mg, 0.054 mmol) and 4-aminobenzoic acid (295 mg, 2.15mmol) in 2 mL of anhydrous DMF was stirred at 135 °C. The clear red solution turned deep blue after 5h and was cooled to r.t. before quenching with aqueous saturated NaHCO<sub>3</sub>. The aqueous layer was extracted with DCM (3 x 100 mL) and the combined organic extracts were dried over MgSO<sub>4</sub>, filtered and concentrated under reduced pressure. The resulting waxy material was placed under high vacuum until DMF was completely removed and a violet-blue solid was obtained. Purification by column chromatography on silica gel (DCM: MeOH 9:1) provided **dye 3** as a blue solid (40 mg, 96%).

2.1.7. **Dye 4:** *N,N'*-Di-(2,6-diisopropylphenyl)-2-aminobenzoic acid-6-bromonaphthalene-1,4,5,8-tetracarboxylic acid bisimide (*Br,N*-NDI)

View Article Online  
DOI: 10.1039/C7GC00125H

For reaction (vi) (Fig. 1), in a 25 mL Schlenk-flask purged with Argon a mixture of *N,N'*-Di-(2,6-diisopropylphenyl)-2-aminobenzoic acid-6-bromonaphthalene-1,4,5,8-tetracarboxylic acid bisimide (*Br,N*-NDI) (75 mg, 0.094 mmol) and 4-aminobenzoic acid (129.2 mg, 0.94 mmol) in 4 mL anhydrous NMP was stirred at 150 °C. The clear violet solution turned deep blue after 48h and was cooled to r.t. before quenching with aqueous saturated NaHCO<sub>3</sub>. The aqueous layer was extracted with DCM (3 x 100 mL) and the combined organic extracts were dried over MgSO<sub>4</sub>, filtered and concentrated under reduced pressure. The resulting waxy material was placed under high vacuum until NMP was completely removed and a blue solid was obtained. Purification by column chromatography on silica gel (DCM:MeOH 9:1) provided **dye 4** as a blue solid (73 mg, 90%).

## 2.2. Preparation of BiVO<sub>4</sub> photocatalyst

### 2.2.1. BiVO<sub>4</sub> powders

BiVO<sub>4</sub> powders were prepared following a previously optimized receipt.<sup>30</sup> Bismuth nitrate pentahydrate (Bi(NO<sub>3</sub>)<sub>3</sub>·5H<sub>2</sub>O) and ammonium metavanadate (NH<sub>4</sub>VO<sub>3</sub>) both from Sigma Aldrich were used as BiVO<sub>4</sub> precursors. No further purification of the reagents were performed. In a first step, 3.7 mmol of Bi(NO<sub>3</sub>)<sub>3</sub>·5H<sub>2</sub>O, 3.7 mmol of NH<sub>4</sub>VO<sub>3</sub> and 12 mmol of ammonium carbonate were dissolved in 75 mL of 1M HNO<sub>3</sub>. After 30 min of stirring at room temperature, a clear solution was obtained (pH = 0). The mixture was then heated for 12h at 180 °C in a 100 mL Teflon-lined stainless steel auto-clave under autogenous pressure. The precipitate was filtered, washed three times with distilled water and then with ethanol, and dried at r.t. The dry samples were annealed at 450 °C for 2 h. All the chemicals used in the experiments were also of an analytical grade and bi-distilled water was used for the preparation of the solution.

### 2.2.2. BiVO<sub>4</sub> films

BiVO<sub>4</sub> films were prepared by a spin-coating method into FTO-substrates over a 2 x 3 cm<sup>2</sup> area. The FTO-glass substrates were cleaned in acetone and ethanol by means of ultrasonication, and then washed with bi-distilled water before the BiVO<sub>4</sub> deposition. For a typical deposition, two different solutions were prepared by dissolving 2.97 g of Bi(NO<sub>3</sub>)<sub>3</sub>·5H<sub>2</sub>O in 15 mL of acetic acid and 1.624 g of vanadyl acetylacetonate (VO(acac)<sub>2</sub>) in 75 mL of acetylacetonone. Such amounts are doubled with respect to a recently published receipt,<sup>6</sup> in order to increase the thickness of the film by each single spin-coating step. The mixture of those solutions, which has a Bi/V atomic ratio of 1, was subjected to ultrasonication for 30 min at 59 Hz to obtain a stable sol that was then spin-coated at 500 rpm for 10 s into the FTO-glass substrates. After drying at 150 °C for 5 min on a hot plate, the films were annealed at 400 °C for 10 min in order to induce the BiVO<sub>4</sub>

crystallization. After natural cooling at r.t., this procedure was repeated one more time to increase the film thickness. The electrodes were finally annealed at 400 °C for 2 h.

View Article Online  
DOI: 10.1039/C7GC00125H

### 2.3. Preparation of naphthalenediimides decorated BiVO<sub>4</sub>.

The anchorage of the dye molecules to both the BiVO<sub>4</sub> powder and film (see Fig. 2) was accomplished by modified dip-coating techniques based on previously reported procedures.<sup>32, 33</sup> Different solvent systems and conditions (i.e. Method A and Method B shown in Table 1) were used depending to the solubility of the organic substrates. In a typical reaction, the dye was dissolved in dry solvent and added *via canula* over 0.10 g of finely ground BiVO<sub>4</sub> powder previously charged in a 100 mL round-bottom flask, equipped with a reflux condenser and maintained under inert atmosphere. The resulting suspension was stirred overnight and the solid material was separated by filtration on a fritted glass funnel, wash with 20 mL of the respective hot solvent solution and dried at 100 °C for 1 h.

**Table 1:** Experimental conditions for the sensitization of BiVO<sub>4</sub> with different dyes

Method	Dye	Solvents	Dye Concentration [mM]	Stirring Temperature [°C]
A	1	Toluene : DMF (50:3 v/v)	50	120
B	2, 3 or 4	Ethanol	10	90

### 2.4. Physicochemical characterization of naphthalenediimides-BiVO<sub>4</sub>

Crystalline structure and morphology of pristine and impregnated BiVO<sub>4</sub> powders were characterized by X-ray diffraction (XRD with a X'Pert PRO diffractometer) analysis by Cu-K $\alpha$  X-ray tube,  $\lambda = 1.54 \text{ \AA}$  with 40 kV of accelerating voltage and Field Emission Scanning Electron Microscopy (FESEM) images performed with a Zeiss Merlin microscope.

UV-Vis reflectance spectra (% R) were collected with a spectrophotometer (Cary 500 by Varian) by using an integration sphere. The surface composition of the samples was characterized by X-ray photo-electron-spectroscopy (XPS, PHI5000 VersaProbe). The XPS analyses were carried out with a VG Escalab 200-C X-ray photo-electron-spectrometer, with a non-monochromatic Mg-K source. A pass energy of 20 eV, a resolution of 1.1 eV, and a step of 0.2 eV were used for the high-resolution spectra. The effects of sample charging were eliminated by referring the spectral line shift to /a C1s binding energy value of 284.6 eV.

### 2.5. Water oxidation activity of naphthalenediimides decorated BiVO<sub>4</sub>

#### 2.5.1. Photocatalytic Oxygen evolution measurements

The catalytic activity was measured by means of the previously reported Clark cell system.<sup>22</sup> In a typical test, 10 mg BiVO<sub>4</sub> were tested in 11 mL of a 50 mM AgNO<sub>3</sub> solution. Dissolved O<sub>2</sub> (DO)

was measured with a Clark type electrode (InPro 6050/120, Mettler Toledo). Prior to each measurement, O<sub>2</sub> was removed by flowing N<sub>2</sub> through the liquid phase with a positive pressure of 1.05 atm. Then, the reactor was illuminated with simulated solar light (AM 1.5G, 100mW/cm<sup>2</sup>) with a plasma lamp (LIFI STA-40, LUXIM). O<sub>2</sub> production rate (RO<sub>2</sub>) was measured as the slope of the initial portion of DO curves [dDO/dt]<sub>0</sub> and the max value of oxygen (DO\*) was considered as the total oxygen production. A control without catalyst was performed in dark and under illumination in order to determine the increment of DO due to atmospheric oxygen.

### 2.5.2. Photoelectrochemical measurements

Photoelectrochemical (PEC) measurements were run with a standard three-electrode setup in a lab-made cell. An Ag/AgCl (3 M KCl) electrode and a Pt wire were used as reference electrode and counter electrode, respectively. The measurements were recorded with a multichannel VSP potentiostat/galvanostat (BioLogic), equipped with EC-Lab v. 10.1x software for data acquisition. Potentials vs. the Ag/AgCl reference electrode were converted to the reversible hydrogen electrode (RHE) scale by using the Nernst Equation:  $E_{RHE} = E_{Ag/AgCl} + E_{0Ag/AgCl} + 0.059 \text{ pH}$ .  $E_{RHE}$  is the converted potential vs. RHE (e.g.  $V_{RHE}$ ),  $E_{0Ag/AgCl}$  is the standard potential of Ag/AgCl (3 M KCl) at 25 °C, i.e. 0.209 V, and  $E_{Ag/AgCl}$  is the experimental potential measured against the Ag/AgCl reference electrode (e.g.  $V_{Ag/AgCl}$ ). The catalytic activity of BiVO<sub>4</sub> films was tested at pH = 7.0 in 0.1 M sodium phosphate buffer. Linear sweep voltammetry (LSV) curves were performed in the dark and under continuous or chopped simulated solar light, in the range between 0.4  $V_{RHE}$  and 1.6  $V_{RHE}$  (sweep rate of 20 mV s<sup>-1</sup>). The intensity of the light was maintained at 100 mW cm<sup>-2</sup> by adjusting the distance between the light source (i.e. Newport 450 W Xe lamp equipped with an AM 1.5G filter simulating sunlight and a water filter) and the PEC cell. Chrono-amperometry (CA) measurements were performed at 1.23  $V_{RHE}$  over chopped (2 min dark and 2 min light) visible light irradiation. The charge transfer resistance across the semiconductor-electrolyte interface was evaluated by EIS measurements, conducted in the 0.1 Hz to 0.5 MHz frequency range, with an alternating current (AC) amplitude of 25 mV at different applied potentials (i.e. 0.63, 0.93, 1.23 and 1.53  $V_{RHE}$ ). In order to measure the Incident photon-to-electron conversion efficiency (IPCE) spectra, the PEC cell was illuminated using a Newport Xe lamp (150 W) by varying the incident light from 300 nm to 700 nm (step size: 10 nm) by means of a monochromator (Cornestone 130 by Newport), at an applied potential of 1.23  $V_{RHE}$ . In this case, the electrode illuminated area was 1 cm<sup>2</sup> and the light power density was about 1 mW cm<sup>-2</sup>, measured at 390 nm.

### 2.6. Experimental determination of the HOMO and LUMO energy levels

The HOMO and LUMO energy levels and the band gap ( $E_g$ ) between them were determined via cyclic voltammetry (CV) by using the onset potential of the first oxidation and reduction peak,

respectively. The estimations can be done with the empirical relation, shown in equation 1 and 2, including the ferrocene (Fc) oxidation value of 4.8 eV as external standard.<sup>34</sup>  $E_{1/2(\text{Fc})}$  is equal to 0.4 V.<sup>35</sup>

$$E_{\text{HOMO}} = - \left[ \left( E_{\text{OX}} - E_{\frac{1}{2}(\text{Fc})} \right) + 4.8 \right] \text{eV} \quad (1)$$

$$E_{\text{LUMO}} = - \left[ \left( E_{\text{RED}} - E_{\frac{1}{2}(\text{Fc})} \right) + 4.8 \right] \text{eV} \quad (2)$$

Where  $E_{\text{OX}}$  and  $E_{\text{RED}}$  are the onset potentials [ $V_{\text{Ag/AgCl}}$ ] of oxidation and reduction, respectively. The experiments were performed in a three electrodes systems consisting of a Pt wire as the counter electrode, an Ag/AgCl as reference electrode and a glassy carbon working electrode. Three consecutives CVs with a scan rate of 100 mV/min between  $-3 V_{\text{Ag/AgCl}}$  and  $4 V_{\text{Ag/AgCl}}$  were carried out. For the preparation of the sample, 20  $\mu\text{L}$  of a solution containing the dye (10 mg/ml) was dropped on a glassy carbon electrode and left to evaporate in dark conditions. The supporting electrolyte was a solution of 0.1 M tetrabutylammonium hexafluorophosphate (TBAPF<sub>6</sub>) in acetonitrile. To ensure that there is no oxygen in the electrolyte, a purge with nitrogen was performed for 15 min at a flow rate of 24 Nml/min before each measurement.

## 2.7. Computational Details

All calculations were performed using the Gaussian09 series of programs.<sup>36</sup> Full quantum mechanics calculations on the energy levels of the dyes were performed within the framework of density functional theory (DFT) using the BP86<sup>37,38</sup> and PBE<sup>39,40</sup> functionals with the basis set 6-31g(d,p),<sup>41-43</sup> for all the atoms. All geometry optimizations were full, with no restrictions using the Berny algorithm implemented in Gaussian09.<sup>44</sup> The solvent effects of the acetonitrile was computed via the continuum IEF-PCM model.<sup>45</sup>

## 3. Results and Discussion

### 3.1 Synthesis of core-substituted NDIs.

The syntheses of the **dyes 1 - 4** described in this work were performed according to the scheme represented in Fig. 1. The condensation between the commercially available 1,4,5,8-naphthalenetetracarboxylic acid dianhydride and 4-aminopyridine in anhydrous DMF, provided the first target compound **dye 1** with 69 % of yield after several recrystallization steps as confirmed by NMR, FT-IR and MS analyses (see section 2.1.2).

The preparation of the key intermediate (i.e. 2,6-dibromo-naphthalene tetracarboxylic dianhydride) for the syntheses of the **dyes 2 to 4** was accomplished by the bromination of the starting anhydride with dibromoisocyanuric acid (DBI) in oleum. A mixture of poly-brominated products were obtained and were directly employed in the next condensation with 2,6-diisopropyl-aniline. To avoid S<sub>N</sub>Ar reactions, the latter step was performed in acetic acid, where

most amino functions were protonated.<sup>46</sup> The reaction product was isolated with 54% of yield and confirmed by NMR, F-TIR and MS analyses (see supporting information, *SI*).

Subsequently, the substitution of the two bromide substituents was achieved using various reagents to produce the **dyes 2 to 4** (see sections 2.1.5 and 2.1.6). The novel mono- and di-substituted cNDIs (*i.e.* **dyes 2-4**) were selectively prepared from the same intermediate and 4-aminobenzoic acid through an appropriate control of the reaction conditions (time and equivalents of 4-aminobenzoic acid). It is worth to illustrate that the introduction of the NMe<sub>2</sub> functionality by S<sub>N</sub>Ar substitution, occurred unexpectedly from DMF decomposition. Indeed, some literature reports<sup>47, 48</sup> described that under specific reaction conditions DMF could decompose providing a source of -NMe<sub>2</sub> group, which in our case would be the responsible of the second substitution on the naphthalene core.

The purity and composition of all the prepared NDIs were confirmed by NMR and FT-IR spectroscopy as well as by MS characterization (Fig.s S1 to S5 in *SI*) and an excellent yield of the syntheses was obtained: 93%, 96% and 96%, for **dyes 2, 3** and **4**, respectively.

Moreover, the new synthesized NDIs evidence light absorption over a broad range of wavelengths in the UV and Vis ranges (see Fig. S6, *SI*); *i.e.* between 200 and 390 nm for all the dyes and with peaks in the visible region for **dyes 2 to 4**. Indeed, the **dye 1** evidence main adsorption peaks in the UV range, at wavelengths ( $\lambda$ ) of 237 and 350 nm, as expected for core-unsubstituted NDIs.<sup>46</sup> Instead, **dyes 2, 3** and **4** present significant bathochromical shift of the absorption maxima, attaining noticeable visible light harvesting peaks at 520, 600 and 660 nm, respectively, other than in the UV region, because of the different functionalization introduced to the naphthalene core.<sup>46</sup> Interestingly, the **dye 4** practically cover all the solar spectra with a more constant light absorption intensity. The here synthesized core-substituted NDIs are thus suitable to cover the “green gap”, *i.e.* operate at wavelengths longer than 500 nm, hence, being promising materials to be used into photocatalytic systems with other semiconductor materials.

The resulting optical properties of the dyes obviously depend on their HOMO and LUMO energies and band gap (*E<sub>g</sub>*), which also are close-correlated to the photocatalytic behavior of the dye-sensitized BiVO<sub>4</sub> photocatalyst and, therefore, will be introduced above in the section 3.3.

### 3.2 Structural, optical and chemical characterizations of NDI-decorated BiVO<sub>4</sub>.

The efficient anchoring of the NDI dyes onto the BiVO<sub>4</sub> surface was confirmed by XRD, FT-IR, TGA, FESEM and XPS analyses. The quantification of the amount of each dye in the corresponding functionalized material was obtained by thermogravimetric analyses (see Fig.s S7b and S8, *SI*). The highest impregnation, equal to 42 wt%, was obtained with **dye 1**, followed by **dye 4**, **dye 3** and **dye 2** with a 14 wt%, 6 wt% and 3.8 wt%, respectively. The highest impregnation obtained with **dye 1** could be attributed to the highest concentration used during the impregnation, which was 5-fold higher than the one used with **dyes 2 - 4**. Nevertheless, the different functional

groups presents in the **dyes 1 to 4** have also a direct effect on the binding interactions formed with the BiVO<sub>4</sub> surface and, consequently, on the final dye loading.

Previous FT-IR analysis and amines absorption test carried out on BiVO<sub>4</sub> samples revealed the presence of Lewis acid sites on its surface,<sup>49</sup> that are supposed to be the main anchoring moiety during the functionalization of the semiconductor. In the case of the simple core-unsubstituted NDI (**dye 1**), which contains two pyridine moieties, it is possible that this kind of linker established a stronger interaction with the BiVO<sub>4</sub> surface by means of the two exposed aromatic nitrogen atoms. Instead, in the case of the **dyes 2 - 4**, the carboxylic acid functionality, which is the most commonly used anchoring group for dye sensitized solar cells,<sup>33</sup> is envisaged to be the linkage moiety with the BiVO<sub>4</sub> surface.

From a structural and morphological point of view, the bare BiVO<sub>4</sub> powder exhibits a monoclinic scheelite crystalline phase (see FESEM image, Fig. 3a, and XRD spectrum, Fig. 4a). BiVO<sub>4</sub> powder's diffraction peaks were in good agreement with the standard Joint Committee on Powder Diffraction Standards (JCPDS) card No. 14-0688 (space group: I2/a, a = 5.195, b = 11.701, c = 5.092, β = 90.38 °) and shows the characteristic peak splitting diffractions at 2θ = 18.5, 35 and 46 °.<sup>30</sup> No traces of scheelite–tetragonal or zircon–tetragonal phases are observed in the diffraction pattern, which points out the high selectivity of the chosen synthesis method. As shown in Fig. 3, after the impregnation with the dyes, the level of coverage of the BiVO<sub>4</sub> crystals varies with the dye used. In particular, the surface of the BiVO<sub>4</sub> crystals impregnated with the **dye 1** is completely covered by a needle-like crystalline structure (Fig. 3b). Coherently, the X-ray diffraction of the BiVO<sub>4</sub> + **dye 1** powder shown in Fig. 4a evidences three peaks at 19.2, 22.8 and 23.6 ° that correspond to the crystalline structure of **dye 1**, which XRD complete spectrum is exhibited in Fig. S7c (SI). In contrast to **dye 1**, **dyes 2 - 4**, have an amorphous structure, forming an external layer on the photocatalyst that fill the BiVO<sub>4</sub> inter-particles spaces. The image corresponding to the BiVO<sub>4</sub> powder impregnated by the **dye 4** is exhibited as an example in Fig. 3c, which is representative of what was observed after the impregnation with **dyes 2** and **3**, as well. Fig. 3c shows the BiVO<sub>4</sub> crystals with grain boundaries that are less defined than such reported in Fig 3a (for bare BiVO<sub>4</sub>) and are evidently embedded in the non-crystalline shell constituted by the dye. Indeed, due the covering of the BiVO<sub>4</sub> powder with the **dyes 2 to 4** less defined BiVO<sub>4</sub> XRD peaks were observed (Fig. 4a), which again is in agreement with a good coverage of the BiVO<sub>4</sub> crystals by these dyes.

The UV-Vis spectra, in reflectance percentage (% R), of the bare BiVO<sub>4</sub> in comparison with the dye-anchored powders are shown in Fig. 4b. These curves are inversely proportional to the absorption spectrum. As expected and in agreement with previous results, the impregnation with the **dyes 2 - 4** increases the absorption region of BiVO<sub>4</sub> to the visible region. This was not

observed with **dye 1**, which mainly absorbs in the UV-region (see Fig. S6). Interestingly, the **dye 3** maintains the absorption in the UV-region, whereas **dyes 2** and **4** showed less absorption than bare BiVO<sub>4</sub> in the range of  $\lambda < 500$  nm.

The surface coverage of the BiVO<sub>4</sub> with the dye is confirmed by the XPS spectra as well (Fig. 5). The intensities of Bi 4f y V 2p spectra, corresponding to elements present only in BiVO<sub>4</sub> molecule, decreases in the order: bare BiVO<sub>4</sub> > BiVO<sub>4</sub> + **dye 3** > BiVO<sub>4</sub> + **dye 2** > BiVO<sub>4</sub> + **dye 1** > BiVO<sub>4</sub> + **dye 4**. From the C 1s spectra of the samples, three peaks are observed, where the peak at 284 eV is attributed to adventitious carbon contamination. In addition, the peaks, observed in the positions 286 eV and 288 eV for C 1s and 532 eV and 533 eV for O 1s, are attributed to the organic C-O and C=O bonds, respectively, and are present (as expected) only in the dye-impregnated powders. Moreover, in the O 1s spectra (Fig. 5b), the peak at 530 eV represents the binding energy of oxygen in metal oxides that, in this case and in line with the previous results, shows the highest intensity for the bare BiVO<sub>4</sub> sample. Finally, the highest intensity for the N 1s high resolution XPS spectra, presented in Fig. 5c, was observed for **dye 1**, followed by **dye 4**, **dye 3** and **dye 2**; interestingly, following the same trend observed in the weight percentage of the dyes loaded into the BiVO<sub>4</sub> powder measured by TGA.

### 3.3 Water oxidation photocatalytic performances of NDI decorated BiVO<sub>4</sub> particles

The photocatalytic activity of the bare and dye-impregnated BiVO<sub>4</sub> powders was measured by means of a Clark type photo-reactor (see Fig. 6a), where atmospheric oxygen was stripped by a constant nitrogen flow which kept a positive pressure (1.05 bar) inside the reactor. Dissolved oxygen curves are shown in Fig. 6b, which were obtained in the course of the experiment with a Clark electrode. After 10 minutes under dark conditions, the reactor was illuminated with 1 sun of irradiance and, in that instant, the curves show a sudden increment in the oxygen production. It is worth noting that the slight increment of the oxygen in dark conditions is due to the baseline of atmospheric O<sub>2</sub>. The oxygen evolution rate (R<sub>O<sub>2</sub></sub>) and the maximum evolved oxygen (DO\*) are reported in Fig. 6c. R<sub>O<sub>2</sub></sub> were calculated as the slope of the first stage of the increasing section of DO curves (10 min < t < 15 min), the values are plotted in Fig. 6c.

It is worth noting, that there is either no correlation between the DO\* and the R<sub>O<sub>2</sub></sub>, nor between the catalytic performance and the dye loading into the BiVO<sub>4</sub>, as it has been observed in previous works by using MnOx and [Ru(bpy)<sub>3</sub>]<sup>2+</sup> for the OER, where a linearity between these parameters was found.<sup>50</sup> This is an indication of the fact that each dyes has a different interaction and effect on the BiVO<sub>4</sub> photocatalyst surface.

In addition, the experiments in the Clark reactor revealed that, although the R<sub>O<sub>2</sub></sub> of the BiVO<sub>4</sub> does not shown a particular improvement induced by any of the dyes, the BiVO<sub>4</sub> + **dye 3** sample exhibits the maximum oxygen production. It was even 75 % higher than the bare BiVO<sub>4</sub>, whereas the DO\* obtained by the impregnation of the **dyes 1**, **2** and **4** remained lower than that of bare

BiVO<sub>4</sub>. This result agrees with the UV-Vis spectrum of **dye 3** (Fig. 4b), which showed that the dye impregnated powder can absorb in the visible region but without reducing the absorbance in the UV region, which could mean that the light harvesting of BiVO<sub>4</sub> is not blocked by the dye. In contrast to the BiVO<sub>4</sub> samples containing the **dyes 2** and **4**, which also showed an increased UV and Vis light absorption, respectively, but a poorer reacting performances, the **dye 3** seems to have a better electronic interactions with BiVO<sub>4</sub>, which is reflected by a higher total oxygen production.

### 3.4 Energy levels of NDIs and water oxidation mechanism of BiVO<sub>4</sub> + dye powder photocatalyst

To better understand the interaction between BiVO<sub>4</sub> and the different dyes, the energy levels of HOMO and LUMO of **dyes 1 - 4** were calculated and compared with the energy levels of BiVO<sub>4</sub> and the water splitting reaction. The values of the energy levels were determined by two methods, experimentally and theoretically, the latter by means of DFT calculations (see section 2.7).

Table 2 compares the energy of the HOMO and LUMO orbitals determined experimentally and computationally through two different non-hybrid DFT functionals (BP86 and PBE), which were shown to be relatively accurate for predicting HOMO-LUMO gaps.<sup>51</sup>

**Table 2:** Values of HOMO and LUMO energies and band gap (E<sub>g</sub>) for **dyes 1 - 4** obtained by both experimental (Exp.) and theoretical methods: BP86 and PBE functionals. See further details in Table S1 and Fig. S9 (SI).

	HOMO [eV]			LUMO [eV]			E <sub>g</sub> [eV]	
	Exp.	BP86	PBE	Exp.	BP86	PBE	Exp.	BP86
<b>Dye 1</b>	-6.35	-6.20	-6.04	-3.66	-4.13	-4.04	2.69	2.07
<b>Dye 2</b>	-5.53	-5.49	-5.39	-3.95	-4.01	-3.90	1.58	1.48
<b>Dye 3</b>	-5.16	-4.94	-4.84	-3.65	-3.69	-3.58	1.51	1.26
<b>Dye 4</b>	-5.40	-5.09	-4.98	-3.82	-3.88	-3.78	1.57	1.21

The experimental and computed energies of the HOMO follow the same trend: **dye 1** << **dye 2** < **dye 4** < **dye 3**. The computed absolute values are qualitatively, if not quantitatively, close the experimental ones, mutually supporting both methodologies (see Table 2). The largest discrepancy between the experimental and calculations appears for the LUMO energy of **dye 1**, which is the lowest among the series of dyes according to DFT methods, following the same trend as the HOMO energies, but it is one of the highest according to experimental method. Apart from this case, the calculated LUMO levels are in rather good agreement with experimental values obtained with experimental method. It is important to note that time-independent quantum methods were found to give a poorer description of unoccupied than occupied orbitals.<sup>51</sup>

Fig. 7 depicts the DFT computed frontier molecular orbitals and their respective position with respect to BiVO<sub>4</sub> and water splitting reaction by using the average value between the BP86 level and experimental data (see Table S1, SI). Within the series of studied dyes, the addition of electron-donating substituents to the naphthalene core in **dyes 2 - 4** destabilizes significantly the energy of the HOMO with respect to **dye 1**. For **dyes 2 - 4**, the HOMO is delocalized over the 4-rings core forming  $\pi$ -antibonding interactions with the electron-donating substituents, whereas in **dye 1** the HOMO is delocalized over the two pyridine substituents. Roughly, the energy of the HOMO (**dye 1** << **dye 2** < **dye 4** < **dye 3**) correlates with the donor ability of the corresponding dye substituents (H < Br < N(H)ArCOOH < NMe<sub>2</sub>). DFT calculations show the same destabilization trend for the LUMO energies. However, the energy of the LUMO is less altered, and consequently, the energy gaps for the dyes with electron-donating substituents (**dyes 2 - 4**) are significantly narrower than for **dye 1**. This trend is also observed for experimental energy gap values despite the above mentioned discrepancy on the LUMO energies for **dye 1**.

In order to establish if the **dyes 1 - 4** work as sensitizer, some physical requests have to be satisfied. The electron transfer from the donor to the acceptor requires that the lowest unoccupied molecular orbital (LUMO) level of the dye is above that of the BiVO<sub>4</sub> (*i.e.* its CB), and hole transfer from the acceptor to donor requires that the highest occupied molecular orbital (HOMO) level of the dye is above that of the BiVO<sub>4</sub> (*i.e.* its VB), in order to fulfill the energy requirements and thus to generate the photocurrent. From Fig. 7 we can infer that **dyes 1 - 4** fulfil those requisites.

A Z-scheme type photosystem, which has demonstrated enhanced photocatalysts performances by mimicking the natural photosynthesis in Photosystem II,<sup>52</sup> is possible with the here presented dyes and could explain why the WO performance of the BiVO<sub>4</sub> + **dye 3** couple is better than such with the other dyes. As schematically depicted in Fig. 8a, the forward intramolecular and interfacial hole/electron transfer processes can be summarized as follows: (1) upon light irradiation the dye produces a long-lived charge separated excited state (dye + hv  $\rightarrow$  dye\*), which eventually could evolve to the minimum on the triplet potential energy surface, and it results in a photo-excited electron, dye(e<sup>-</sup>), and a hole, dye(h<sup>+</sup>); (2) the BiVO<sub>4</sub> also absorbs radiation injecting an electron in the conduction band, BiVO<sub>4</sub>(e<sup>-</sup>), and generating a hole in the valence band, BiVO<sub>4</sub>(h<sup>+</sup>), which is able to oxidize water (BiVO<sub>4</sub> + hv  $\rightarrow$  BiVO<sub>4</sub>\*); (3) electron-hole recombination to the excited dye in order to preserve the hole in the BiVO<sub>4</sub>, so that it can act as a water oxidation catalyst (BiVO<sub>4</sub>\* + dye(h<sup>+</sup>)  $\rightarrow$  BiVO<sub>4</sub>(h<sup>+</sup>) + dye(e<sup>-</sup>)); (4) electron injection into the electron acceptor (AgNO<sub>3</sub> salt) or into the conduction band of the semiconductor oxide (dye(e<sup>-</sup>) + Ag<sup>+</sup>  $\rightarrow$  dye + Ag<sup>0</sup>, or dye(e<sup>-</sup>) + BiVO<sub>4</sub>  $\rightarrow$  dye + BiVO<sub>4</sub>(e<sup>-</sup>)). The non-optimal performance of the overall process can be attributed to the radiative and non-radiative recombination within the BiVO<sub>4</sub> oxide (3' in Fig. 8a). However, the presence of the dye can hinder the electron-hole recombination

within the BiVO<sub>4</sub> oxide by accepting the photo-excited electron of BiVO<sub>4</sub> in the hole produced in the dye HOMO after its photo-excitation. This process is likely to be maximized when the conduction band of the oxide and the HOMO of the dye are close in energy. Thus, since **dye 3** has the strongest e- donor substituent (NMe<sub>2</sub>) in the naphthalene core what destabilizes significantly the energy of the HOMO, it shows the lowest differences between HOMO and CB energy levels. Therefore, a better electron transfer with BiVO<sub>4</sub> with respect to the other dyes is allowed, which could explain the better performances obtained with the BiVO<sub>4</sub> + **dye 3** in the Clark-reactor experiments.

From the Fig. 7 it can also be noticed that holes transfer from the BiVO<sub>4</sub> to the **dye 3** cannot cause the water splitting reaction in the surface of the dye, because the energetic level of holes in the HOMO of **dye 3** are not enough oxidant to induce e- transfer from the water to that dye, with a consequent impossibility to achieve water splitting and O<sub>2</sub> evolution. In order to better clarify the actual mechanism of charges transfer and the real possibility to implement the here developed dyes in a photoelectrochemical device, the PEC behavior of the most promising **dye 3** coupled with a BiVO<sub>4</sub> photo-electrode has been evaluated, and the results are presented in the next section 3.5.

### 3.5 Photoelectrochemical application of the NDI dye 3-anchored BiVO<sub>4</sub> film

In order to assess the possible practical application and stability of the NDIs as well as to confirm the capability of the best NDI dye to enhance the reaction kinetics, the performance of a BiVO<sub>4</sub> + **dye 3** film was evaluated and compared to such of bare BiVO<sub>4</sub> for the overall water splitting reaction. The PEC cell containing a 0.1 M Na-phosphate buffer solution (pH 7). From both chopped and continuous light LSV scans (Fig. 9a), a gradual increase of the photocurrent under simulated sunlight irradiation (100 mW cm<sup>-2</sup>) is observed for both samples, with an onset potential at about 0.6 V<sub>RHE</sub>. A reduction of the theoretical redox potential for water oxidation (E° = 1.23 V<sub>RHE</sub>) indicates that part of the energy required for the reaction is provided by the simulated sunlight.

The quite low photocurrent density (at 1.23 V<sub>RHE</sub>) of the BiVO<sub>4</sub> film (~ 0.03 mA·cm<sup>-2</sup>), is in agreement with previous data in the literature for high area electrodes such the ones here employed (2 x 3 cm<sup>2</sup>).<sup>6</sup> Nonetheless, the implementation of the here developed **dye 3** over a broad electrode surface was consciously made to test a system closer to a practical case. As noticed from Fig. 9, the generated photocurrent varies considerably between the bare and impregnated BiVO<sub>4</sub> films. The BiVO<sub>4</sub> + **dye 3** film shows a photocurrent of 0.3 mA cm<sup>-2</sup> at 1.23 V<sub>RHE</sub>, which correspond to more than ten-fold the photocurrent generated with the bare BiVO<sub>4</sub>. In addition, the photocurrent of the BiVO<sub>4</sub> + **dye 3** film does not arrive to a plateau, such as the bare BiVO<sub>4</sub> does, but continuous an increment by increasing the potential, reaching up to 0.53 mA cm<sup>-2</sup> at 1.6 V<sub>RHE</sub>.

Fig. 9b shows the photocurrent density stability of the studied photo-anodes as a function of time. To perform this, the samples were illuminated in cycles of two minutes of darkness and simulated solar light irradiation. The photocurrent shows an instantaneous increment when the irradiation begins, then shows a slight decrease and stabilizes to a steady state condition after few seconds. The  $\text{BiVO}_4 + \text{dye 3}$  film shows a more pronounced spike respect to the bare  $\text{BiVO}_4$ , showing a slight lower photocurrent than the LSV curves. Such is commonly observed because in chopped LSVs the irradiation time is too short for the sample to reach the steady state condition as well as the continuous increase of the applied potential induces a faster  $e^-$  transport in LSVs than in CAs. However, the enhancement in the photocurrent due to the **dye 3** impregnation is in agreement with the LSV results. It is important to notice that, the photocurrent decreased quickly down to zero when the light is turned off, confirming the effective photocatalytic (and not only catalytic) activity of both studied films.

In order to identify the portion of the solar spectra that is actually working in the  $\text{BiVO}_4 + \text{dye 3}$  film in comparison to the bare  $\text{BiVO}_4$  film, the photo-response of the different photo-anodes have been evaluated through IPCE spectra at an applied potential of  $1.23 V_{\text{RHE}}$  (Fig. 10a). IPCE curves revealed that both the  $\text{BiVO}_4$  and  $\text{BiVO}_4 + \text{dye 3}$  have a relevant efficiency in the UV-Vis region of sunlight up to a maximum of 500 nm. The maximum IPCE was obtained at 320 nm for both samples and is of about 28 % and 49 % for the pristine  $\text{BiVO}_4$  and the **dye 3**-impregnated film, respectively. Hence, there was no evidence of an increase of the action spectra of  $\text{BiVO}_4$  in the visible range due to the presence of the dye, which is actually in agreement with the previous discussion related to the position of the HOMO level of this dye and the inability to achieve water oxidation by the holes on its surface. Nevertheless, the enhanced activity of the  $\text{BiVO}_4 + \text{dye 3}$  material is also confirmed by the IPCE measurements.

The better feature of the **dye 3** impregnated film could be explained by the different transport properties of such electrode, which can be observed from the Nyquist plots of the electrochemical impedance spectroscopy measurements under simulated sunlight illumination reported in Fig. 10b. The smaller impedance values reported by the  $\text{BiVO}_4 + \text{dye 3}$  film than by the bare  $\text{BiVO}_4$ , at the different applied potentials, indicate a faster electron transfer (higher reaction kinetics at the electrode/electrolyte interface) by reducing  $e^-/h^+$  recombination's on the  $\text{BiVO}_4$  surface.<sup>6, 53, 54</sup> For instance, at  $1.23 V_{\text{RHE}}$  the charge transfer resistance of the  $\text{BiVO}_4 + \text{dye 3}$  film ( $\sim 136 \Omega$ ) is less than a half of such of the bare  $\text{BiVO}_4$  ( $\sim 300 \Omega$ ).

The mechanism of improvement of charge transfer in the surface of the  $\text{BiVO}_4$  by the **dye 3** can be explained through two phenomena. Other than the previously explained Z-scheme that is possible between the  $\text{BiVO}_4$  and **dye 3**, the **dye 3** could also act as an enhancer of electrons mobility and, consequently, of charges separation and photocurrent generation by a higher

availability of holes in the BiVO<sub>4</sub> surface able to react with water. The latter phenomena is similar to such previously observed for BiVO<sub>4</sub> films with reduced graphene oxide<sup>55</sup> or in TiO<sub>2</sub> porous films impregnated with a conductive polymer (*i.e.* polyaniline).<sup>29</sup> In the present case, the unique characteristic provided by the aromatic diimide moiety (*i.e.* NDI) and the core-substituted derivatives, which have been already exploited as electron-acceptor moieties in artificial light-harvesting systems such as dye sensitized solar cells, is responsible for the semiconducting property of the **dye 3**.<sup>56</sup> Indeed, the planar geometry of NDIs and their low reduction potential have been reported to provide a large driving force for the charge separation process,<sup>56, 57</sup> since NDIs can be reversibly reduced to stable radical anions, under mild conditions.

The possible mechanism by which **dye 3** improve the photo-electrocatalytic activity of BiVO<sub>4</sub> under sunlight irradiation is schematized in Fig. 8b. When the BiVO<sub>4</sub> + **dye 3** heterostructure is irradiated by UV-Vis light, the **dye 3** absorbs photons and electrons in the HOMO can be excited to the LUMO. In the same manner, BiVO<sub>4</sub> absorbs UV-Vis photons and electrons in the BiVO<sub>4</sub> VB can be excited to its CB, thereby leaving holes at its surface able to split water to O<sub>2</sub>. Then, through the Z-scheme process, electrons in the CB of BiVO<sub>4</sub> can be injected in the HOMO of **dye 3**, because they are at a higher energy level than the BiVO<sub>4</sub> VB; otherwise, electrons in the **dye 3** LUMO can be injected into the BiVO<sub>4</sub> CB and then, due to the electromagnetic forces induced by the applied bias, be injected into the FTO conductive substrate. These processes are beneficial for an efficient charge carrier's separation because they induce an increased electrons mobility and transport in the BiVO<sub>4</sub> CB.<sup>29, 56</sup> Hence, **dye 3** likely hinders the recombination of the e<sup>-</sup>/h<sup>+</sup> pairs and lengthen the lifetime of the charge carriers, consequently improving the charge separation and photocatalytic activity of the BiVO<sub>4</sub> photocatalyst. Thus, the fast transferred electrons into the FTO conductive substrate are then conducted through the external electrical circuit to the Pt cathode where the H<sub>2</sub> evolution reaction takes place.

#### 4. Conclusions

In this work, a new series of core-substituted NDIs was designed, with the aim of obtaining tunable absorption properties that overlap with all the solar spectrum and bearing appropriate functionalities to provide efficient and stable linkage on the surface of the BiVO<sub>4</sub> water-splitting photocatalyst. Four different molecules were successfully synthesized achieving excellent yields (~ 69 % for **dye 1** absorbing UV-light; and > 93 % for **dyes 2 to 4** absorbing visible light) as it was confirmed by NMR, FT-IR and GC-MS analyses. The surface functionalization of BiVO<sub>4</sub> has been accomplished by an easy and low-cost room temperature dip-coating technique. The successful anchoring, as well as the stability of the photocatalyst-dye interactions, have been successfully confirmed by TGA, FT-IR, XRD, XPS and optical analysis.

The diversely sensitized BiVO<sub>4</sub> samples were tested for the photocatalytic oxygen evolution process under simulated sunlight conditions by employing two different systems: a Clark-type reactor with a sacrificial e<sup>-</sup> acceptor (AgNO<sub>3</sub>) and a photoelectrochemical water splitting cell. The optimum dye-sensitized catalytic systems was proven to be such including **dye 3** on BiVO<sub>4</sub>, which provided a remarkable enhancement in the O<sub>2</sub> evolution from both quantitative and kinetic point of views, confirming the effectiveness of the catalytic system here designed. The superior activity of the BiVO<sub>4</sub> + **dye 3** system has been ascribed to two phenomena: first, a Z-scheme<sup>4, 58, 59</sup> mechanistic approach is possible due to the right position HOMO and LUMO energy levels of the **dye 3** with respect to those of the BiVO<sub>4</sub> (*i.e.* CB and VB), as determined by DFT calculations and experimental data; moreover, we considered that the ability of the here developed organic dyes to delocalize the electronic charge and enhance electrons transport towards the FTO substrate could be an additional key factor that minimizes recombination processes in the BiVO<sub>4</sub> + **dye 3** water oxidation photoanode. The here proposed approach opens new perspectives in the investigation of a different series of dye molecules (namely, NDIs) that are low-cost, because do not contain expensive noble metals, and are able to improve the activity of photocatalysts for different sunlight driven applications, such as waste water treatment and organic contaminants degradation, other than the production of solar fuels by water splitting mechanisms.

### Acknowledgements

Sitaramanjaneya Mouli Thalluri, Mauro Raimondo and Salvatore Guastella are acknowledged for the technical support during the synthesis of the BiVO<sub>4</sub> powders, FESEM and XPS measurements, respectively. This work has been funded by the EU Commission, 7th European Framework Program (NMP-2012), Project Eco2CO<sub>2</sub>, Grant Agreement number 309701. Computational research was supported by the Spanish Ministry of Science and Innovation (CTQ2014-52774-P) and the Generalitat de Catalunya (2014SGR199 and XRQTC). The CTQC/URV authors acknowledge the Spanish Ministerio de Economía y Competitividad (CTQ2013-43438-R) and the Generalitat de Catalunya (2014SGR670) for financial support.

### Supporting Information (SI)

Supplementary Information is available: NMR, FT-IR spectra and MS analyses of dye 1 to 4 and Br,Br-NDI; photographs of dyes solutions in acetonitrile, their UV-Vis spectra and molecular structures; FT-IR spectra and TGA of BiVO<sub>4</sub> + dyes heterostructures; theoretical and experimental data related to the calculation of the energy levels of the dyes. See DOI: 10.1039/x0xx00000x.

### Author Contributions

S. Hernández optimized the synthesis of BiVO<sub>4</sub> powders and films with advises of N. Russo; she also designed, coordinated and supervised the photo and electro catalytic water splitting experiments. S. Hernández, C. Ottone and N. Russo performed and analyzed the chemical-physical and optical characterizations of the bare and dye-sensitized BiVO<sub>4</sub> samples. C. Ottone experimentally determined the HOMO and LUMO energy levels of the dyes. K. Tolod did the photoelectrochemical tests. S. Proto and S. Castellón designed and developed the organic synthetic routes to obtain the core-substituted NDIs. S. Proto and C. Godard optimized the grafting procedure of the dyes on BiVO<sub>4</sub> powders. S. Proto and M. Díaz de los Bernardos performed FT-IR, NMR, MS and TG characterizations under the supervision of C. Godard. A. Solé-Daura and J. J. Carbó performed and analyzed the DFT calculations. G. Saracco and C. Claver ideated and planned the research work. All authors discussed and analyzed the results, contributed to writing and approved the final manuscript.

## References

1. J. Barber, *Chemical Society Reviews*, 2009, 38, 185-196.
2. N. S. Lewis and D. G. Nocera, *Proceedings of the National Academy of Sciences*, 2006, 103, 15729-15735.
3. C. Acar, I. Dincer and G. F. Naterer, *International Journal of Energy Research*, 2016, 40, 1449-1473.
4. R. Abe, *Journal of Photochemistry and Photobiology C: Photochemistry Reviews*, 2010, 11, 179-209.
5. Y. Park, K. J. McDonald and K.-S. Choi, *Chemical Society Reviews*, 2013, 42, 2321-2337.
6. S. Hernández, G. Gerardi, K. Bejtka, A. Fina and N. Russo, *Applied Catalysis B: Environmental*, 2016, 190, 66-74.
7. L. Xia, J. Bai, J. Li, Q. Zeng, L. Li and B. Zhou, *Applied Catalysis B: Environmental*, 2017, 204, 127-133.
8. X. Meng and Z. Zhang, *Journal of Molecular Catalysis A: Chemical*, 2016, 423, 533-549.
9. A. Kudo, K. Omori and H. Kato, *Journal of the American Chemical Society*, 1999, 121, 11459-11467.
10. D. K. Zhong, S. Choi and D. R. Gamelin, *Journal of the American Chemical Society*, 2011, 133, 18370-18377.
11. B. Zhou, J. Qu, X. Zhao and H. Liu, *Journal of Environmental Sciences*, 2011, 23, 151-159.
12. D. Rössler, R. Kontic and G. R. Patzke, *Materials Chemistry and Physics*, 2012, 135, 457-466.
13. S. Obregón, A. Caballero and G. Colón, *Applied Catalysis B: Environmental*, 2012, 117-118, 59-66.
14. G. Xi and J. Ye, *Chemical Communications*, 2010, 46, 1893-1895.
15. C. Martínez Suarez, S. Hernández and N. Russo, *Applied Catalysis A: General*, 2015, 504, 158-170.
16. L. Wenjun, W. Zhiqiang, W. Lijuan, L. Zhaosheng, Y. Tao and Z. Zhigang, *Journal of Physics D: Applied Physics*, 2010, 43, 405402.
17. G. Li, D. Zhang and J. C. Yu, *ChemInform*, 2008, 39, no-no.
18. K. Tolod, S. Hernández and N. Russo, *Catalysts*, 2017, 7, 13.
19. B. Anke, M. Rohloff, M. G. Willinger, W. Hetaba, A. Fischer and M. Lerch, *Solid State Sciences*, 2017, 63, 1-8.

20. H. Ye, J. Lee, J. S. Jang and A. J. Bard, *The Journal of Physical Chemistry C*, 2010, 114, 13322-13328. View Article Online  
DOI: 10.1039/C7GC00125H
21. J. Quiñonero, T. Lana-Villarreal and R. Gómez, *Applied Catalysis B: Environmental*, 2016, 194, 141-149.
22. S. M. Thalluri, S. Hernández, S. Bensaid, G. Saracco and N. Russo, *Applied Catalysis B: Environmental*, 2016, 180, 630-636.
23. D. Pei and J. Luan, *International Journal of Photoenergy*, 2011, 2012.
24. W. J. Youngblood, S.-H. A. Lee, K. Maeda and T. E. Mallouk, *Accounts of chemical research*, 2009, 42, 1966-1973.
25. Y. Zhao, J. R. Swierk, J. D. Megiatto, B. Sherman, W. J. Youngblood, D. Qin, D. M. Lentz, A. L. Moore, T. A. Moore, D. Gust and T. E. Mallouk, *Proceedings of the National Academy of Sciences*, 2012, 109, 15612-15616.
26. J. R. Swierk, D. D. Méndez-Hernández, N. S. McCool, P. Liddell, Y. Terazono, I. Pahk, J. J. Tomlin, N. V. Oster, T. A. Moore, A. L. Moore, D. Gust and T. E. Mallouk, *Proceedings of the National Academy of Sciences*, 2015, 112, 1681-1686.
27. H. Yu, R. Shi, Y. Zhao, G. I. N. Waterhouse, L. Z. Wu, C. H. Tung and T. Zhang, *Advanced Materials*, 2016, 28, 9454-9477.
28. D. Tang, H. Zhang, H. Huang, R. Liu, Y. Han, Y. Liu, C. Tong and Z. Kang, *Dalton Transactions*, 2013, 42, 6285-6289.
29. D. Hidalgo, S. Bocchini, M. Fontana, G. Saracco and S. Hernandez, *RSC Advances*, 2015, 5, 49429-49438.
30. S. M. Thalluri, C. Martinez Suarez, S. Hernández, S. Bensaid, G. Saracco and N. Russo, *Chemical Engineering Journal*, 2014, 245, 124-132.
31. D. D. Perrin, W. L. F. Armarego and D. R. Perrin, *Purification of laboratory chemicals*, Pergamon Press, Oxford; New York, 1980.
32. K. Moller and T. Bein, 1998, DOI: 10.1021/cm980243e.
33. J. Rochford, D. Chu, A. Hagfeldt and E. Galoppini, *Journal of the American Chemical Society*, 2007, 129, 4655-4665.
34. J. Zhang, C. Yu, L. Wang, Y. Li, Y. Ren and K. Shum, *Scientific Reports*, 2014, 4, 6954.
35. V. V. Pavlishchuk and A. W. Addison, *Inorganica Chimica Acta*, 2000, 298, 97-102.
36. G. W. T. M. J. Frisch, H. B. Schlegel, G. E. Scuseria, M. A. Robb, J. R. Cheeseman, G. Scalmani, V. Barone, B. Mennucci, G. A. Petersson, H. Nakatsuji, M. Caricato, X. Li, H. P. Hratchian, A. F. Izmaylov, J. Bloino, G. Zheng, J. L. Sonnenberg, M. Hada, M. Ehara, K. Toyota, R. Fukuda, J. Hasegawa, M. Ishida, T. Nakajima, Y. Honda, O. Kitao, H. Nakai, T. Vreven, J. A. Montgomery, Jr., J. E. Peralta, F. Ogliaro, M. Bearpark, J. J. Heyd, E. Brothers, K. N. Kudin, V. N. Staroverov, R. Kobayashi, J. Normand, K. Raghavachari, A. Rendell, J. C. Burant, S. S. Iyengar, J. Tomasi, M. Cossi, N. Rega, J. M. Millam, M. Klene, J. E. Knox, J. B. Cross, V. Bakken, C. Adamo, J. Jaramillo, R. Gomperts, R. E. Stratmann, O. Yazyev, A. J. Austin, R. Cammi, C. Pomelli, J. W. Ochterski, R. L. Martin, K. Morokuma, V. G. Zakrzewski, G. A. Voth, P. Salvador, J. J. Dannenberg, S. Dapprich, A. D. Daniels, O. Farkas, J. B. Foresman, J. V. Ortiz, J. Cioslowski and A. D. J. Fox, *Gaussian 09, revision C.01*, 2010, Gaussian, Inc.: Wallingford CT.
37. J. P. Perdew, *Physical Review B*, 1986, 33, 8822-8824.
38. A. D. Becke, *Physical Review A*, 1988, 38, 3098-3100.
39. J. P. Perdew, K. Burke and M. Ernzerhof, *Physical Review Letters*, 1996, 77, 3865-3868.
40. J. P. Perdew, K. Burke and M. Ernzerhof, *Physical Review Letters*, 1997, 78, 1396-1396.
41. M. M. Francl, W. J. Pietro, W. J. Hehre, J. S. Binkley, M. S. Gordon, D. J. DeFrees and J. A. Pople, *The Journal of Chemical Physics*, 1982, 77, 3654-3665.
42. W. J. Hehre, R. Ditchfield and J. A. Pople, *The Journal of Chemical Physics*, 1972, 56, 2257-2261.
43. P. C. Hariharan and J. A. Pople, *Theoretica chimica acta*, 1973, 28, 213-222.
44. P. Pulay and G. Fogarasi, *The Journal of Chemical Physics*, 1992, 96, 2856-2860.

45. E. Cancès, B. Mennucci and J. Tomasi, *The Journal of Chemical Physics*, 1997, **107**, 3032-3041. View Article Online  
DOI: 10.1039/C7GC00125H
46. C. Thalacker, C. Röger and F. Würthner, *The Journal of Organic Chemistry*, 2006, **71**, 8098-8105.
47. S. Ding and N. Jiao, *Angewandte Chemie International Edition*, 2012, **51**, 9226-9237.
48. B. Basu and S. Kundu, *New Journal of Chemistry*, 2014, **38**, 3367-3370.
49. T. Saison, N. Chemin, C. Chanéac, O. Durupthy, V. Ruaux, L. Mariey, F. Maugé, P. Beaunier and J.-P. Jolivet, *The Journal of Physical Chemistry C*, 2011, **115**, 5657-5666.
50. S. Bensaid, C. Ottone Melis, S. Hernández, M. Armandi, S. Esposito, G. Saracco and B. Bonelli, *Chemical Engineering Journal*, 2017, **311**, 143-152.
51. G. Zhang and C. B. Musgrave, *The Journal of Physical Chemistry A*, 2007, **111**, 1554-1561.
52. A. Iwase, Y. H. Ng, Y. Ishiguro, A. Kudo and R. Amal, *Journal of the American Chemical Society*, 2011, **133**, 11054-11057.
53. D. Hidalgo, R. Messina, A. Sacco, D. Manfredi, S. Vankova, E. Garrone, G. Saracco and S. Hernández, *International Journal of Hydrogen Energy*, 2014, **39**, 21512-21522.
54. S. Hernández, M. Tortello, A. Sacco, M. Quaglio, T. Meyer, S. Bianco, G. Saracco, C. F. Pirri and E. Tresso, *Electrochimica Acta*, 2014, **131**, 184-194.
55. Y. H. Ng, A. Iwase, A. Kudo and R. Amal, *The Journal of Physical Chemistry Letters*, 2010, **1**, 2607-2612.
56. S. V. Bhosale, C. H. Jani and S. J. Langford, *Chemical Society Reviews*, 2008, **37**, 331-342.
57. H. E. Katz, A. J. Lovinger, J. Johnson, C. Kloc, T. Siegrist, W. Li, Y. Y. Lin and A. Dodabalapur, *Nature*, 2000, **404**, 478-481.
58. R. Abe, K. Shinmei, N. Koumura, K. Hara and B. Ohtani, *Journal of the American Chemical Society*, 2013, **135**, 16872-16884.
59. M. Higashi, R. Abe, T. Takata and K. Domen, *Chemistry of Materials*, 2009, **21**, 1543-1549.

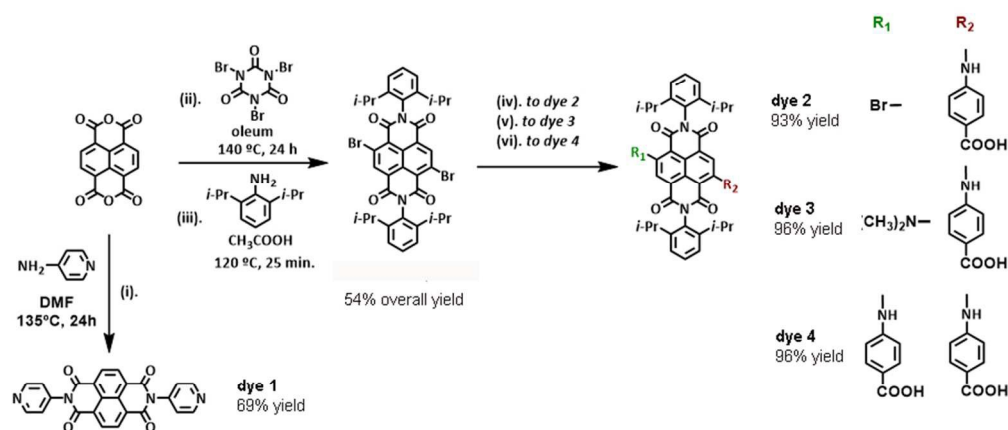


Figure 1. Synthetic strategy for the preparation of substituted-Naphtalenediimides. Reagent conditions: (i) 4-Aminopyridine/DMF, 135 °C / 2 4h; (ii) Tribromocyanuric acid/oleum, 140 °C / 24 h; (iii) 2,6-Diisopropylaniline/CH<sub>3</sub>COOH, 120 °C / 25 min; (iv) 10 equiv. of 4-Aminobenzoic acid/DMF, 135°C/2h; (v) 40 equiv. of 4-Aminobenzoic acid /DMF, 135 °C / 5 h; (vi) 40 equiv. of 4-Aminobenzoic acid/DMF, 150 °C / 2 h.

153x76mm (150 x 150 DPI)

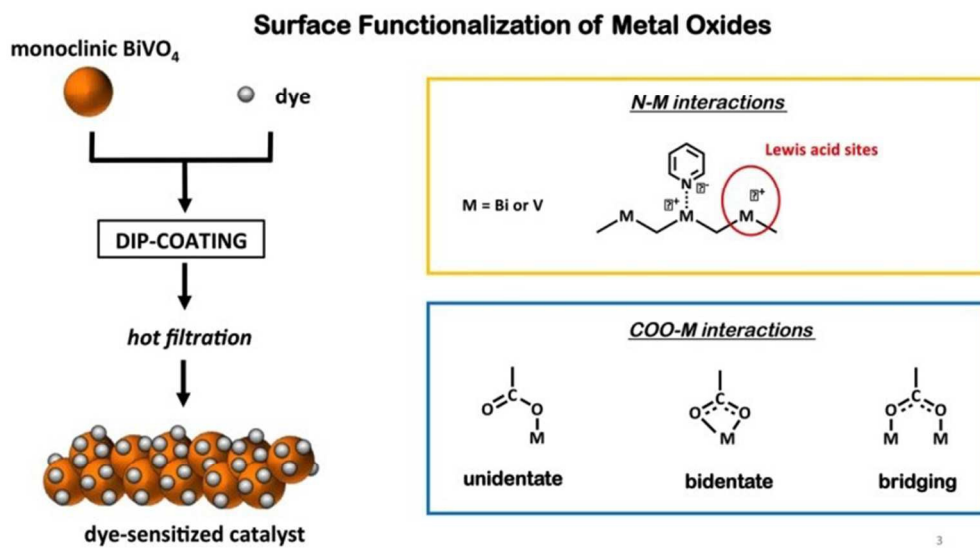


Figure 2. Surface functionalization technique

93x51mm (220 x 220 DPI)

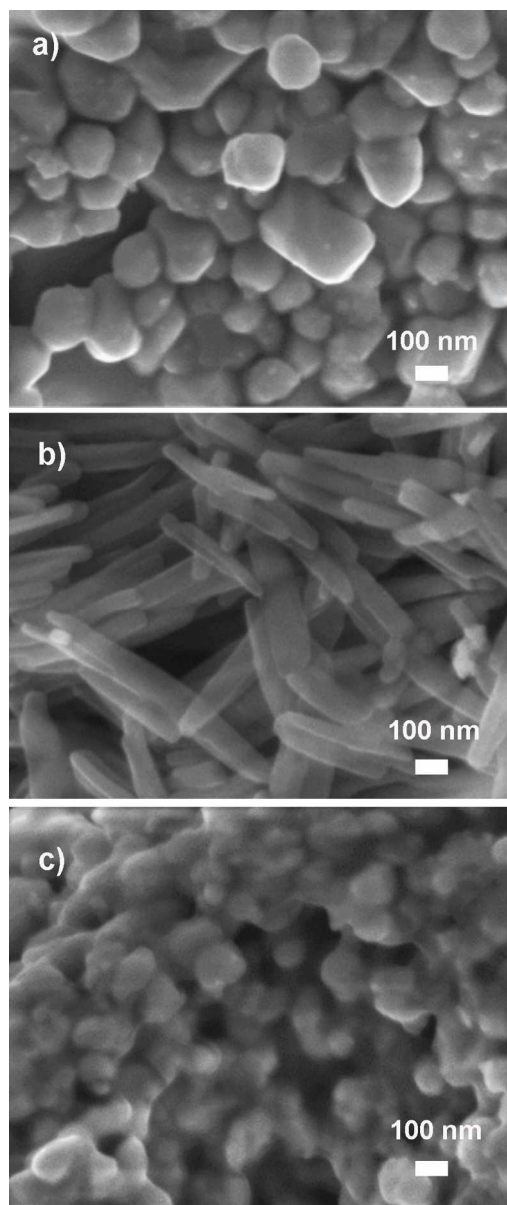


Figure 3. FE-SEM images of (a) pristine  $\text{BiVO}_4$  powder and impregnated with (b) dye 1 and (c) dye 4.

79x189mm (300 x 300 DPI)

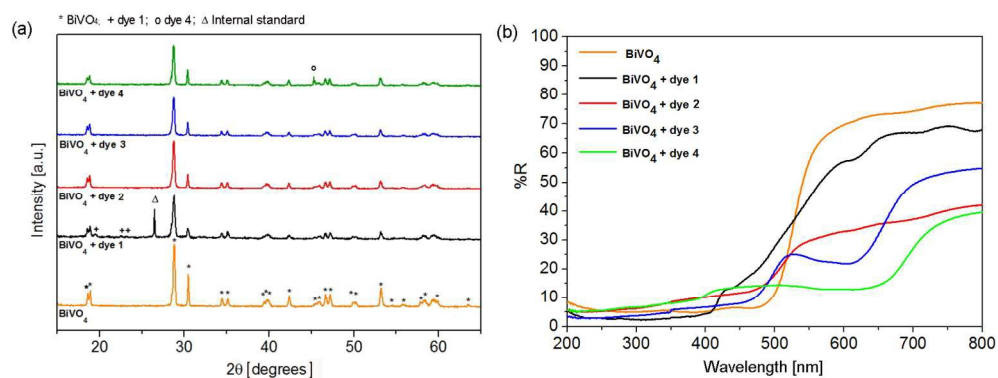


Figure 4: Physicochemical characterization: (a) X-ray diffraction patterns and (b) UV-Vis spectra in total reflectance of the pristine BiVO<sub>4</sub> powder and impregnated with dyes 1 to 4.

154x64mm (300 x 300 DPI)

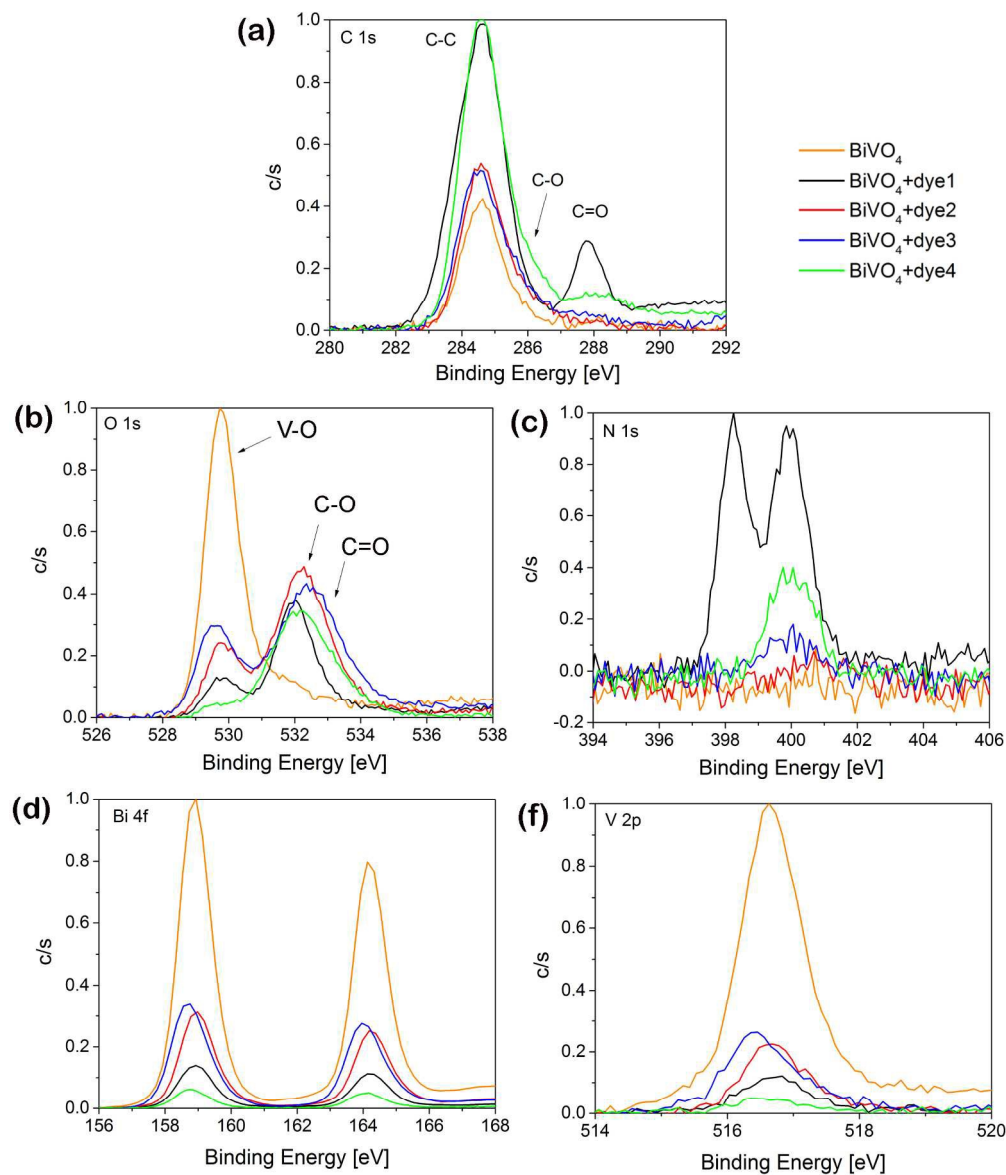


Figure 5. High resolution (a) C 1s, (b) O 1s, (c) N 1s, (d) Bi 4f and (e) V 2p XPS spectra of the pristine  $\text{BiVO}_4$  powder and after the impregnation with dyes 1 to 4.

209x251mm (300 x 300 DPI)

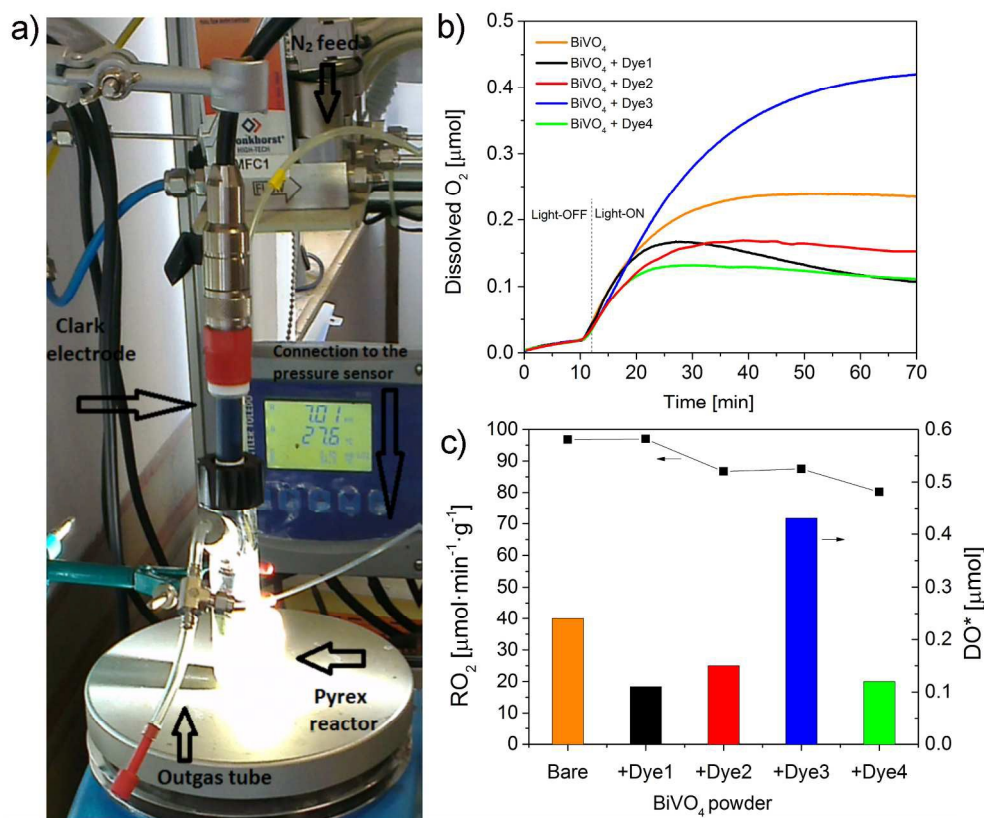


Figure 6. Photocatalytic water oxidation measurements. (a) Picture of the Clark-cell system in the lab and comparison of the (b) oxygen evolution curves of the pristine BiVO<sub>4</sub> and impregnated with the different dyes and (c) the Clark-type cell parameters of oxygen evolution rate ( $R_{O_2}$ ) and maximum dissolved oxygen ( $DO^*$ ).

188x159mm (300 x 300 DPI)

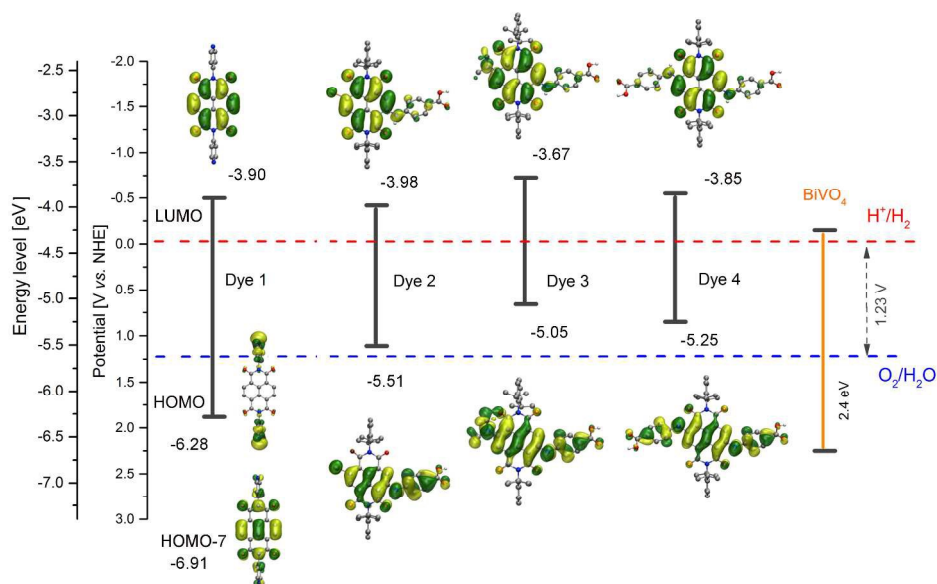


Figure 7. Energy levels of the different dyes and BiVO<sub>4</sub>, including BP86 isodensity surfaces for the computed HOMO and LUMO of the different dyes. Hydrogen atoms are omitted for clarity.

296x181mm (300 x 300 DPI)

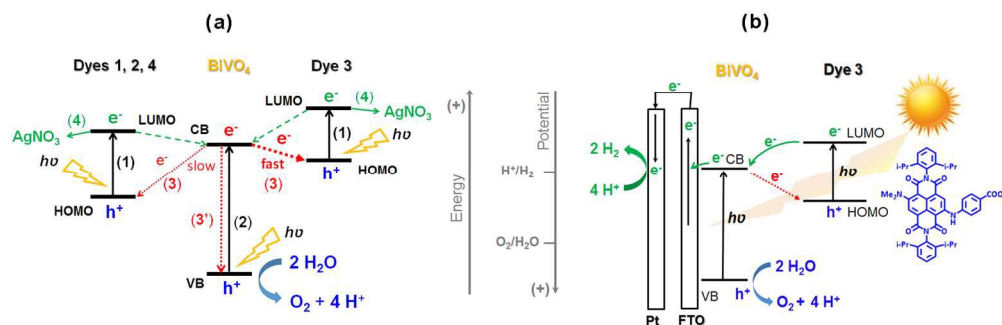


Figure 8. Conceptual representation of the mechanisms of UV-Vis light absorption, charge carriers generation, transfer and separation in the BiVO<sub>4</sub> + dye photocatalytic systems. (a) Z scheme-type mechanism for the photochemical water oxidation reaction under the sacrificial electrons acceptor (AgNO<sub>3</sub>) of the photocatalysts in the powder form. (b) Combined mechanism of charges generation, separation and reaction in the overall water splitting photoelectrochemical cell exploiting the BiVO<sub>4</sub> + dye 3 photoanode.

160x52mm (300 x 300 DPI)

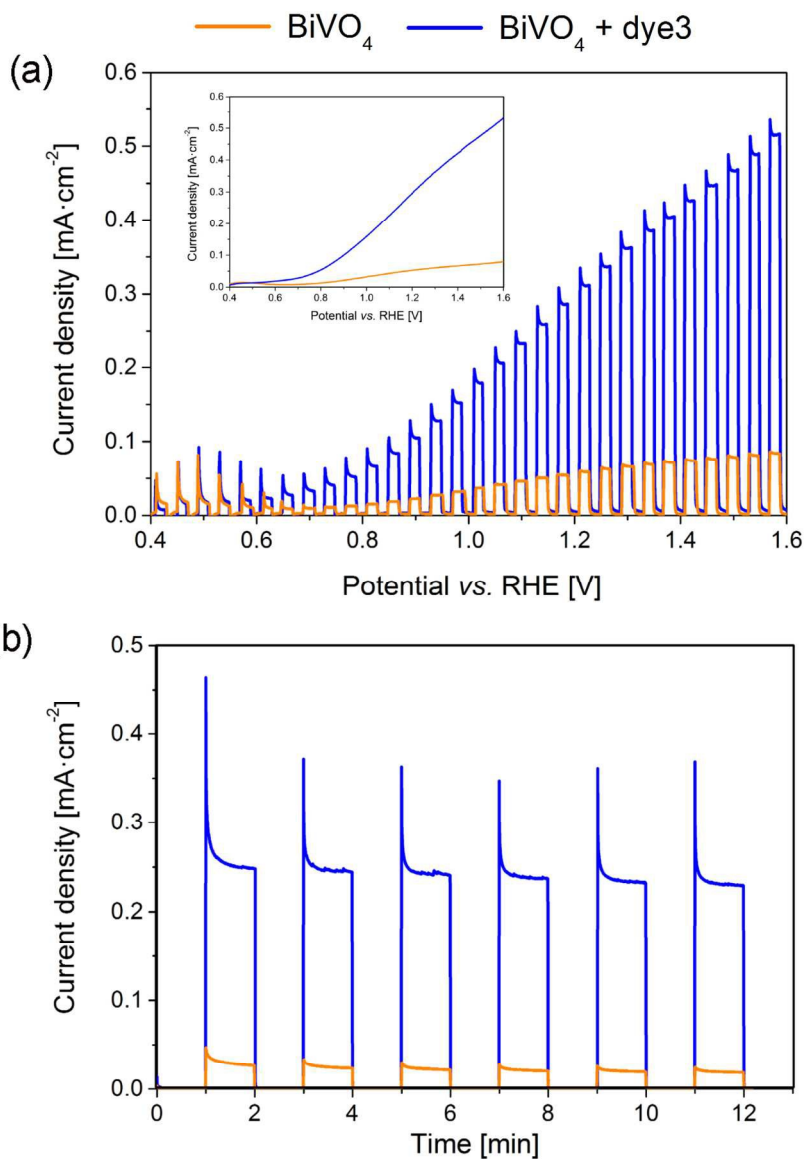


Figure 9. Photoelectrochemical characterizations for the samples:  $\text{BiVO}_4$  film (yellow line) and  $\text{BiVO}_4$  film impregnated with dye 3 (blue line). (a) LSV curves under chopped and continuous (inset) visible light irradiation and (b) CA curves under chopped visible light irradiation at a constant applied potential of 1.23  $V_{\text{RHE}}$ . Active area of the photoanodes:  $6\text{ cm}^2$ .

108x156mm (300 x 300 DPI)

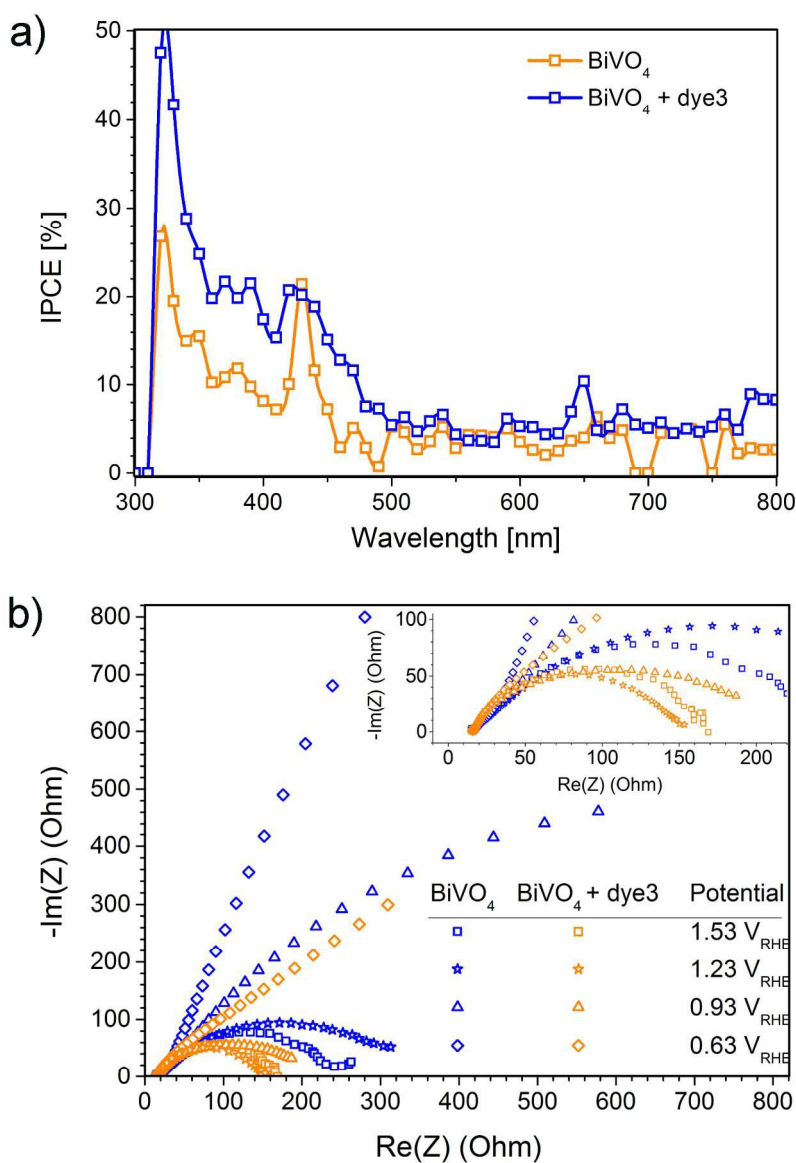
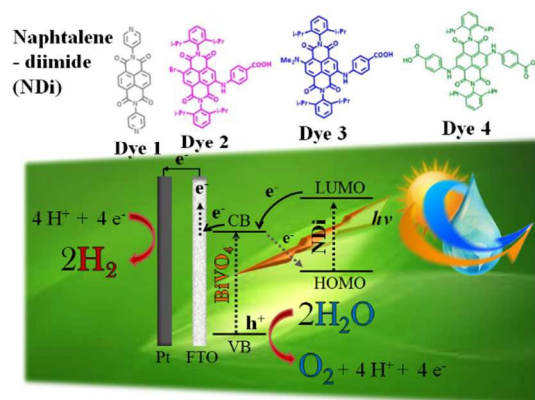


Figure 10. (a) IPCE spectra recorded by varying the wavelength of the incident light from 300 nm to 800 nm at an applied potential of 1.23 V<sub>RHE</sub>. (b) EIS Nyquist plots at different applied potentials under simulated sunlight irradiation. Legend: BiVO<sub>4</sub> (yellow line and symbols) and BiVO<sub>4</sub>+dye 3 (blue line and symbols).

162x237mm (300 x 300 DPI)



Novel photocatalytic system exploiting BiVO<sub>4</sub> coupled to smartly-designed noble-metal-free core-substituted naphthalenediimides for the sunlight-driven water splitting reaction.